Chemical routes to materials

Acetic acid and propionic acid decarboxylation on Mg(OH)$_2$ nanoclusters: a density functional theory study

Duwage C. Perera[1] (iD), Jinasena W. Hewage[2] (iD), and Jayendran C. Rasaiah[1,*] (iD)

[1] *Department of Chemistry, University of Maine, Orono, USA*
[2] *Department of Chemistry, University of Ruhuna, Matara, Sri Lanka*

ABSTRACT

Theoretical analysis of the energetics and mechanism of a reaction can guide the selection of a catalyst from a set of similar candidates and avoid the need for lengthy experimental trials. In this work, a catalyst for the decarboxylation of acetic acid (AA) to methane and carbon dioxide was selected from a set of related magnesium hydroxide [Mg(OH)$_2$]$_n$ (n = 1–9) nanoclusters. Density functional theory (DFT) was used to follow the energetics, mechanism, and stereochemical details of the reaction. It was found that the n = 5 nanocluster had the best performance of the set. For this nanocluster, the decarboxylation reaction proceeded through a single transition state (TS), in contrast to an intermediate and two TSs for the free gas-phase catalytic reaction or decarboxylation with a (MgO)$_4$ catalyst. Inspection of AA adsorbed on the [Mg(OH)$_2$]$_5$ cluster shows the favorable structural orientation of the acid, which facilitated decarboxylation via a single activated state, bypassing the intermediate and one of the TSs. We hypothesized that the decarboxylation of propionic acid to ethane and carbon dioxide should also occur via a single TS with the same catalyst, which was confirmed by a separate DFT study. The [Mg(OH)$_2$]$_5$ clusters have potential use as a coating for textiles to catalyze the decomposition of propionic acid in sweat.

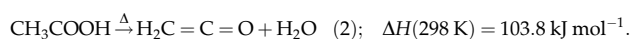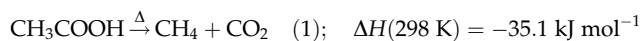
GRAPHIC ABSTRACT

Pathway for AA decarboxylation on [Mg(OH)$_2$]$_5$
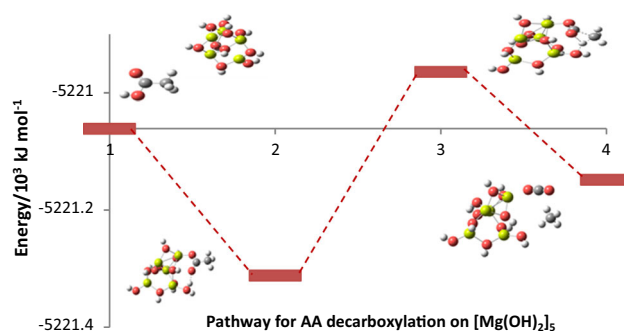
Introduction

The catalytic behavior and adsorption properties of carboxylic acid on metal and metal oxide surfaces have drawn the attention of researchers across the globe. Biomass is one of the most sustainable green energy resources to overcome the problem of fossil fuel depletion along with environmental pollution. One potential problem is the presence of an excessive amount of acids, alcohols, and ether in the bio-oil produced from thermochemical conversions of lignocellulosic biomass. This causes some major drawbacks such as high viscosity, low stability, low heating value, and low pH in the production of high-quality fuel. Therefore, it is important to upgrade bio-oil by reducing/eliminating these compounds. Acetic acid (AA) can be considered as a model acid present in unprocessed bio-oil. Therefore, studying the decomposition of AA is important in upgrading the quality of bio-oil [1, 2]. Acetic acid is a typical weak acid and an important starting material for the production of vinyl acetate and acetic anhydride for the synthesis of long-chain carboxylic acids and many other organic compounds. Additionally, the catalytic decomposition of AA has been identified as a model for eco-friendly treatment for air pollution and wastewater. The decomposition characteristics of the persistent organics in wastewater can be evaluated by studying the AA decomposition [3].

The gas-phase thermal decomposition of AA occurs via both decarboxylation (reaction 1) and dehydration (reaction 2).

$$CH_3COOH \xrightarrow{\Delta} CH_4 + CO_2 \quad (1); \quad \Delta H(298\,K) = -35.1\,kJ\,mol^{-1}$$

$$CH_3COOH \xrightarrow{\Delta} H_2C = C = O + H_2O \quad (2); \quad \Delta H(298\,K) = 103.8\,kJ\,mol^{-1}.$$

Experimental studies by Blake et al. [4, 5] and Bamford et al. [6] concluded that the decarboxylation of AA in the gas phase was a first-order reaction and dehydration was a second-order reaction with activation energies of 259.4 kJ/mol and 282.4 kJ/mol, respectively, at temperatures of 770–920 °C in the absence of a catalyst. However, theoretical studies by Ruelle [7] disagreed with the experimental studies; the barriers they calculated using the MP2/6-31G level of theory were 376.6 kJ/mol for reaction (1) and 325.5 kJ/mol for reaction (2). The calculation was subsequently reexamined by Nguyen [8, 9], who obtained 301 kJ/mol and 317 kJ/mol as activation energies for the decarboxylation and dehydration reactions, respectively. The adsorption of AA and decarboxylation reaction (1) was also studied both theoretically and experimentally using Co [10], Pt [11], and TiO$_2$ [12] catalysts as well as others depending on the application of interest. Hamid et al. studied the photocatalytic conversion of AA on co-catalyst-loaded TiO$_2$, and the amount of CO$_2$ and CH$_4$ formed is increased in the order of Ag/TiO$_2$ < Au/TiO$_2$ < Rh/TiO$_2$ < RuO$_2$/TiO$_2$ < IrO$_2$/TiO$_2$ < Pt/TiO$_2$ [13]. A literature survey reveals that AA absorbs on most of the metal oxide surfaces via a

carbonyl stretching or OH stretching bonds. Liao et al. studied the adsorption and photoreactions of AA on TiO$_2$ at 308 K temperature using Fourier-transformed infrared (FTIR) spectroscopy. Comparing the absorption frequencies, they concluded that molecular AA can absorb on TiO$_2$ surface via hydrogen bonding or by Lewis acid–base interactions (carbonyl stretching) [14]. According to the FTIR study of Martin et al., AA is strongly absorbed on a MgO surface (with recorded bands corresponding to OH stretching) and dissociates to form surface magnesium carboxylates. These carboxylates produce CO$_2$ when the system is outgassed at high temperatures [15]. Verma and Kishore studied the catalytic decomposition of AA on Ru and Ru/MgO clusters theoretically using density functional theory (DFT) and found that OH cleavage pathway is favorable for AA decomposition over both catalysts, and Ru/MgO shows better catalytic properties than bare Ru. AA adsorption energies are recorded to be $-$ 21.04 kJ/mol and $-$ 72.74 kJ/mol for Ru and Ru/MgO, respectively. The decomposition of AA is more likely to produce CO$_2$ and CH$_4$ than acetaldehyde. However, the reaction pathway has several intermediates [16].

Another DFT study by Verma and Kishore recently on the kinetics of non-catalytic reactions (1) and (2) calculated the activation energy of the decarboxylation reaction as 291 kJ/mol using the B3LYP/6-31 $G(d)$ and 305 kJ/mol in M06-2X/6-31 $G(d)$ levels of theory in the 298–900 K temperature range. They also concluded the reaction is kinetically unfavorable in this temperature range. The gas-phase decarboxylation reaction proceeds by converting *cis*-CH$_3$COOH into *trans*-CH$_3$COOH in the first step and produces CH$_4$ and CO$_2$ in the second step. They calculated the rate constants for both steps as 1.31E+03 s^{-1} and 1.71E−34 s^{-1}, respectively, at 298 K using the B3LYP/6-31G(d) level of theory. Lower rate constant shows the unfavorability of the second step at 298 K. However, the rate constants increased significantly to 5.81E+09 s^{-1} and 7.31E−03 s^{-1}, respectively, when the temperature was increased to 900 K [17]. This highlights the importance of an effective catalyst to perform the decarboxylation reaction of AA at 298 K.

Theoretical DFT studies of the decarboxylation reaction using magnesium oxide catalyst have concluded that the acid was chemisorbed on the (MgO)$_4$ cluster with an adsorption energy of $-$ 197 kJ/mol before decarboxylation occurred via an intermediate and two transition states (TSs), with an energy barrier of

415 kJ/mol from the adsorbed state at room temperature. The favorable adsorption geometry of the AA molecule occurs with adjacent Mg and O atoms on (MgO)$_4$ cluster. Here, the (MgO)$_4$ cluster acts as a destructive adsorbent to produce CO$_2$ and CH$_4$ [18]. A literature survey reveals a tremendous number of studies carried out on the catalytic decomposition reaction of AA. To the best of our knowledge, those studies show that there is more than one intermediate in the AA decomposition (specifically decarboxylation) reaction pathway.

Magnesium hydroxide, Mg(OH)$_2$, nanocluster catalysts have not been used to study the AA decarboxylation reaction theoretically. It is an inorganic, white solid of interest in many applications in science and industry. It is environmentally friendly and can be used as an antibacterial agent, in packaging, as a fire-extinguishing agent, and also as an agent in wastewater treatment [19–22]. Different methods such as hydrothermal processing [23, 24], water-in-oil microemulsion processing [25], and high-gravity reactive precipitation [26] are used to synthesize magnesium hydroxide crystals and nanoparticles with different sizes and morphologies [27–30]. Its mechanical, catalytic, optical, and electronic properties increase with decreasing the particle size into nano-size range along with an increase in the surface-to-volume ratio [31]. The high surface area and high surface reactivity make these clusters an effective adsorbent. The electronic structure of magnesium hydroxide involves only s–p orbital electrons, which makes it relatively easy to study through the process of decarboxylation of acetic acid using the current state-of-the-art quantum chemistry. An important motivation to study the Mg(OH)$_2$ catalyst is that it is less toxic than (MgO)$_4$ [21, 32], and it is potentially useful as a coating agent for textiles to decompose propionic acid (PA) that is chemically similar to AA and is one of the components of sweat. Another is that the catalytic power of Mg(OH)$_2$ relative to MgO for this reaction is unknown, and the detailed mechanism of decarboxylation of acetic acid absorbed on the magnesium hydroxide has not been compared with the acid absorbed on magnesium oxide clusters and with decarboxylation of the acid in the gas phase, all of which are of intrinsic chemical interest.

Koper et al. in 2003 have found that metal oxides and metal hydroxides including MgO and Mg(OH)$_2$ can be used as destructive adsorbents for biological and chemical contaminations [33]. The term

destructive adsorbent implies its ability to adsorb and chemically destroy the incoming adsorbate simultaneously. For example, the degradation of Sarin, isopropyl methylphosphonofluoridate ($C_4H_{10}FO_2P$) in the presence of brucite (layered structure of $(Mg(OH)_2)$ catalyst, involves physisorption and dissociative chemisorption has been investigated in a recent DFT study [34]

In this work, we study the adsorption of AA on magnesium hydroxide clusters $[Mg(OH)_2]_n$ (n = 1–9) and $(MgO)_4$ using DFT (both with and without dispersion corrections to the B3LYP exchange functional) to understand the differences in the catalytic behavior of specific nanoclusters in the decomposition of acetic acid absorbed on the respective surfaces. It was found that the binding energy of AA on the hydroxide clusters was the largest for n = 5, which is the focus of this study. We compare the decarboxylation of AA with the presence of $[Mg(OH)_2]_5$ cluster and $(MgO)_4$ cluster and without the presence of any cluster in the gas phase. We find that the specific adsorption of AA on the $[Mg(OH)_2]_5$ nanocluster provides a more direct route, via a single TS, to the products that bypass the intermediates that occur with $(MgO)_4$ and $[Mg(OH)_2]_n$ ($n \neq 5$) catalysts and for the gas-phase decarboxylation of AA in the absence of a catalyst. We propose a similar mechanism for the decomposition of propionic acid (PA) to ethane (CH_3CH_3) and CO_2 in the presence of the same $[Mg(OH)_2]_5$ catalyst and confirm it using the same theoretical methods employed for AA. Moreover, this will be a promising decarboxylation reaction pathway to suppress undesirable by-products to produce high-quality vinyl acetate and bio-oil.

This study uses a variety of theoretical tools to provide insight into different decarboxylation mechanisms for AA (and structurally similar acids) on $(MgO)_4$ and $[Mg(OH)_2]_5$ nanocatalysts and highlights a novel feature of a catalyst that avoids the formation of an intermediate to accelerate a reaction without necessarily lowering the energy barriers.

Methods

A range of $[Mg(OH)_2]_n$, (n = 1–9) clusters were investigated to find the structure with the most negative adsorption energy for AA, which was assumed to be the most stable among the absorbed structures. The calculations of the adsorption energy and structure of the acid on each cluster surface were optimized via hybrid DFT with the B3LYP functional and Pople's split valence double-zeta basis set with polarization functions [6-31G(d,p)] and the dispersion term using the D3 version of Grimme's dispersion (GD3) correction for all atoms [35]. The DFT results were also compared with the DGDZVP basis set and the same exchange functional (with and without the dispersion correction) for all atoms in the calculations mentioned above. The ground-state calculations of the energies and structure of the clusters were carried out following the recent work reported by Chen and Dixon [31]. TS optimization and intrinsic reaction coordinate (IRC) search calculations [36, 37] were performed after selecting the cluster with the lowest adsorption energy using the same level of theory [B3LYP/6-31G(d,p)] and the more computationally intensive DGDZVP basis set, which required increased computation time.

The TSs were determined using the synchronous transit-guided quasi-Newton (STQN) method [38] while keeping the cluster frozen. Atomic charges on each atom of adsorbed Structure 3 in Fig. 2 and AA in the gas phase were calculated by fitting the electrostatic potential of the charges in the grid-based method (ChelpG) developed by Breneman et al. [39, 40]. The "atoms in molecules (AIM)" theory developed by Bader [41] was used to examine the topological characteristics of electron density distribution described in the next section. We also calculated the gas-phase AA decarboxylation reaction and AA decarboxylation reaction on $(MgO)_4$ cluster using B3LYP/6-31g(d,p) revisiting our previously published work [18]. All calculations were performed with the Gaussian 09 program package [42].

Results and discussion

Adsorption of AA on the Mg(OH)₂ nanoclusters

Geometry optimization is a major component of computational studies of the structure and reactivity of molecules. It is the process of finding the arrangement of nuclei for which the potential energy is minimized. As a test of our DFT calculations at the B3LYP/6-31G(d,p) level of theory, the adsorption energy of AA on the magnesium hydroxide monomer was determined (Table S1 in the supporting

information, ESM), and the results showed excellent agreement with the coupled cluster single determinant CCSD(T) values.

Hydrolysis of small $(MgO)_n$ clusters to form the corresponding hydroxide is represented by:

$$(MgO)_n + nH_2O \rightarrow Mg_nO_{2n}H_{2n} \equiv [Mg(OH)_2]_n. \quad (3)$$
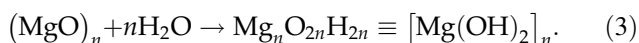
The optimized $[Mg(OH)_2]_n$ structures using the B3LYP/6-31G(d,p) level of DFT for $n = 1$–9 are shown in Fig. 1.

The adsorption energy of AA on each $[Mg(OH)_2]_n$ cluster (E_{ad}) was calculated from:

$$E_{ad} = E_{system} - (E_{AA} + E_{[Mg(OH)_2]n}), \quad (4)$$

where E_{AA} is the energy of structurally optimized AA in the gas phase, $E_{[Mg(OH)_2]n}$ is the energy of the optimized isolated $[Mg(OH)_2]_n$ cluster and E_{system} is the energy of the optimized AA/magnesium hydroxide cluster system. The difference between them is the adsorption or binding energy. The adsorption energies, with and without dispersion correction to the B3LYP exchange functional (B3LYP/6-31G(d,p)), using the same basis set, are shown in Table 1, and the energy variation pattern is plotted in the supplementary material (ESM). The adsorption energies are less negative when the dispersion correction is added to the exchange functional, except for $n = 6$ and 8 where the differences of -4 to -6 kJ/mol, respectively, are relatively small. The difference in the adsorption energy is the largest (20 kJ/mol) for $n = 5$ followed by $n = 1$ and 3, with energy differences of 16 and 11 kJ/mol, respectively. Dispersion forces could be a significant part of adsorption. Grimme's dispersion correction term was added to the basis set to compare the impact of dispersion force in the adsorption energy of AA on $[Mg(OH)_2]_n$ clusters. The lowest adsorption energy or the strongest chemisorption occurs when the cluster size(n) is equal to 5. The next lowest adsorption energies occur when $n = 1$, 3, and 8, respectively. The $[Mg(OH)_2]_5$ cluster was used for all subsequent calculations of the energy intermediates, transition states, and mechanism of the decomposition of AA adsorbed on the cluster.

We calculated energies (energy values are in Table s2 in ESM) of optimized $[Mg(OH)_2]_n$ structures using B3LYP/DGDZVP exchange functional to compare with the literature values [31] and B3LYP/6-31G(d,p) level of theory. Since the values are comparably similar, B3LYP/6-31G(d,p) set was chosen to

Figure 1 Optimized structures of $[Mg(OH)_2]_n$, $n = 1$–9 clusters using the B3LYP/6-31G(d,p) level of DFT.
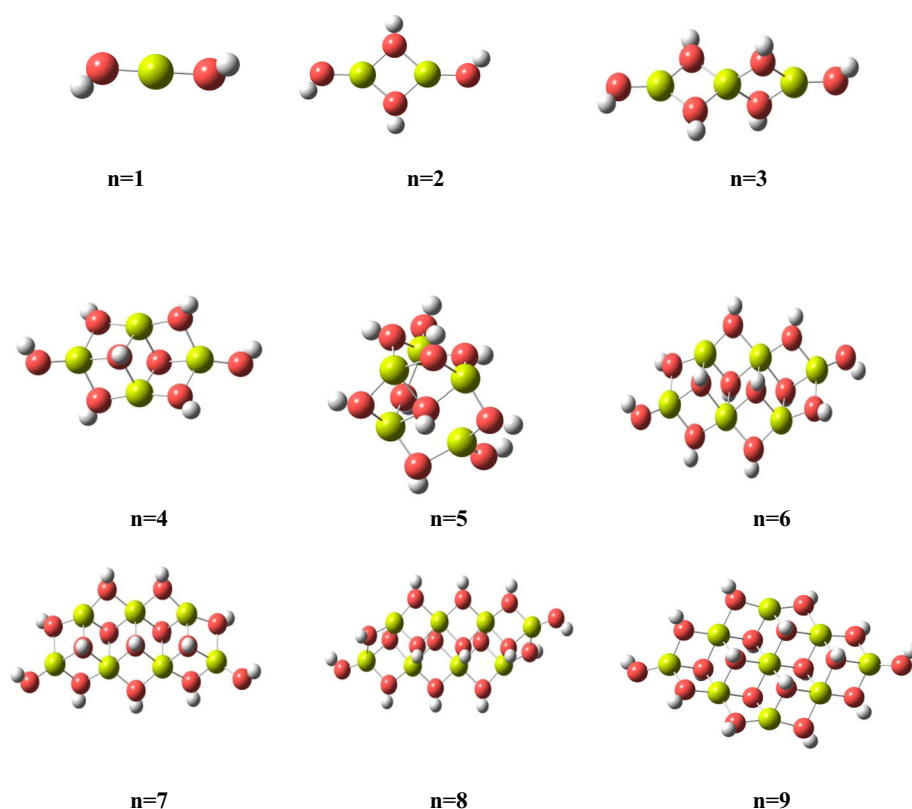
Table 1 Adsorption energies E_{ad} of AA on $[Mg(OH)_2]_n$ in kJ/mol for $n = 1$–9 calculated using the B3LYP/6-31G(d,p), B3LYP/6-31G(d,p) (GD3) and DGDZVP, DGDVP(GD3) exchange functionals and basis sets of DFT

System $[Mg(OH)_2]_n$-AA	N								
Ad. energy (kJ/mol)	1	2	3	4	5	6	7	8	9
B3LYP/6-31G(d,p)	− 225	− 151	− 211	− 99	− 251	− 92	− 140	− 157	− 110
B3LYP/6-31G(d,p) (GD3)	− 209	− 143	− 200	− 98	− 231	− 96	− 137	− 163	− 104
Difference (6-31G(d,p) (GD3)-6-31G(d,p))	16	8	11	1	20	− 4	3	− 6	6
B3LYP/DGDZVP	− 177	− 102	− 167	− 52	− 242	− 44	− 92	− 59	− 71
B3LYP/DGDZVP (GD3)	− 183	− 112	− 181	− 76	− 226	− 73	− 117	− 140	− 90
Difference (DGDZVP (GD3)–DGDZVP)	− 6	− 10	− 12	− 24	16	− 29	− 25	− 81	− 19

calculate the decarboxylation reaction path. The optimized $[Mg(OH)_2]_n$ structures using the DGDZVP basis sets are similar but less negative than the 6-31G(d,p) basis set, while the dispersion correction to the exchange functional makes the energies more negative, as displayed in Table 1. The adsorption energy of AA on the $n = 5$ cluster remains the most negative for both basis sets with and without the dispersion correction for the exchange functional and is within a few kJ/mol (− 231 and − 226 kJ/mol) with the dispersion correction. This difference is mainly due to the different representations of the wave function in two different ways by two basis sets which affects the energy either with or without dispersion correction. However, comparably smaller changes in the adsorption energies (Figure s1 in ESM) and consistency in the effect of the dispersion term to the optimized lowest energies of $[Mg(OH)_2]_n$ clusters show that dispersion does not play a significant role in smaller $[Mg(OH)_2]_n$ clusters.
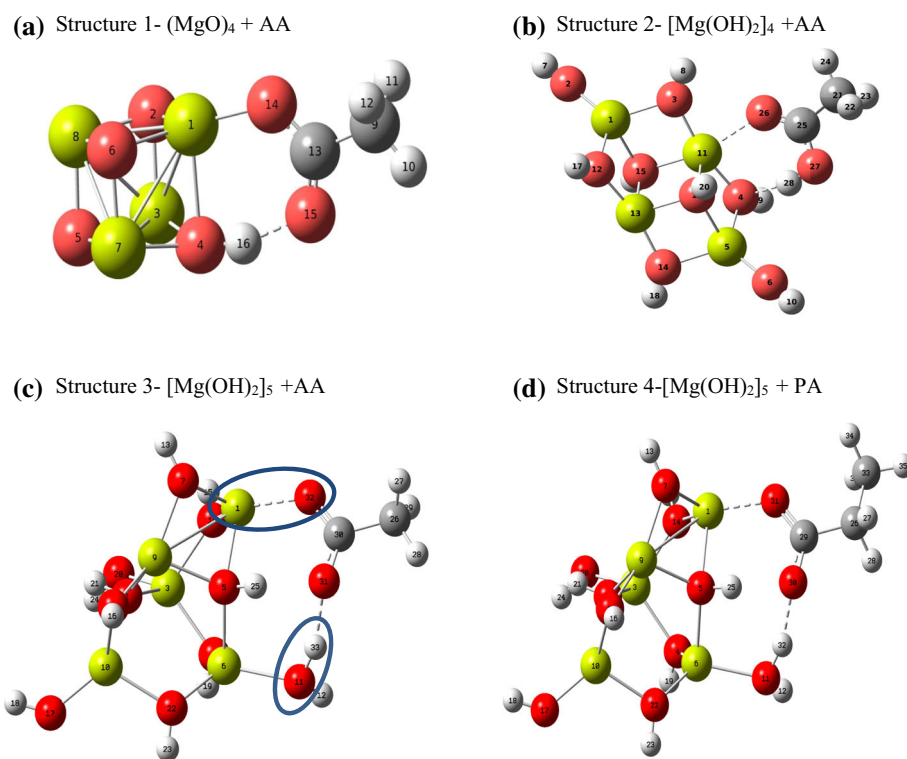
The structural changes caused by the adsorption of AA on the $[(Mg(OH)_2]_5$ catalyst were tracked by following the changes in the bond distances, electron density redistribution, and geometric orientations of AA adsorbed on the nanocluster shown in Structure 3 in Fig. 2. The adsorption of AA on the nanocluster occurs via chemical bonding between 1 Mg–32O and 11O–33H (Structure 3), where the bonding pairs of numbered atoms are encircled in the figure. On absorption, the O–H bond in the acid is elongated from 0.97 to 1.67 Å, while the C–O double bond in the carbonyl group is increased slightly from 1.21 Å to 1.28 Å and the C–O bond attached to the hydroxyl group shortened from 1.35 Å to 1.26 Å, indicating strong adsorption of the acid on the $[(Mg(OH)_2]_5$ cluster. This is accompanied by a slight elongation of

the C–C single bond from 1.50 Å to 1.51 Å in AA, with both the C–O bonds within the acid approaching the same value (Table 2) revealing a potential pathway to form CO_2 and CH_4 in the catalytic decomposition of AA adsorbed on $[(Mg(OH)_2]_5$.

This pathway is unique for $n = 5$, presumably because the adsorption sites on $[(Mg(OH)_2]_5$ are separated by a pair of magnesium and oxygen atoms in the cluster (Structure 3), while the corresponding sites on $[(Mg(OH)_2]_4$ (Structure 2) and $[(MgO]_4$ (Structure 1) are adjacent to each other, as shown in Fig. 2, and discussed below in detail.

Details regarding the adsorption of the AA molecule on the $(MgO)_4$ [18] and the $[Mg(OH)_2]_5$ nanocluster can be observed by comparing Structures 1 and 3 in Fig. 2a. The bonding and C–O–H bond angle of the acidic group within AA differ significantly between the two absorbed structures. The C–O–H angle changes from $\sim$ 119° when AA is adsorbed on $(MgO)_4$ to 133° for $[Mg(OH)_2]_5$. Furthermore, because the O and H atoms of the carbonyl group of AA are bonded to an adjacent pair of Mg and O atoms on $(MgO)_4$, while a pair of O and Mg atoms are present between the corresponding bonding sites on the $[Mg(OH)_2]_5$ adsorbate, the C–O–H angle is larger and closer to the value expected for the decarboxylation TS. These structural dissimilarities lead to differences in the adsorption energies of AA in the presence of the $(MgO)_4$ and $[Mg(OH)_2]_5$ catalysts, and the mechanistic pathways for the decarboxylation that are discussed further in the following sections. Interestingly, the structures of AA adsorbed on the other $[Mg(OH)_2]_n$ nanoclusters with $n = 1$–9, ($n \neq 5$) (e.g., Structure 2 in Fig. 2 and Fig. s2) do not show the stereospecific (spatial and C–O–H angle) binding configurations observed for $n = 5$. Even though $n = 8$

Figure 2 Adsorption of AA on **a** (MgO)$_4$ cluster (Structure 1), **b** [(Mg(OH)$_2$)$_4$ cluster (Structure 2), **c** [(Mg(OH)$_2$)$_5$ cluster (Structure 3) and of PA **d** on [(Mg(OH)$_2$)$_5$ cluster (Structure 4) using the B3LYP/6-31G(d,p) exchange functional and basis set (Mg, O, H, and C are in green, red, light gray, and black, respectively).

(a) Structure 1- (MgO)$_4$ + AA

(b) Structure 2- [Mg(OH)$_2$]$_4$ +AA

(c) Structure 3- [Mg(OH)$_2$]$_5$ +AA

(d) Structure 4-[Mg(OH)$_2$]$_5$ + PA

Table 2 Geometric properties of AA in the gas phase and optimized absorbed states (Structure 3, Figs. 2 and 5), TS, and products (Structures 9 and 10, Fig. 5) on [Mg(OH)$_2$]$_5$ from DFT with B3LYP/6-31G(d,p) level of theory

Geometric property	Structure-bond distances and angles			
	3	9	10	5
D(1C–5C)	1.515	2.076	3.335	1.507
D(8O–5C)	1.280	1.228	1.184	1.210
D(6O–5C)	1.263	1.181	1.152	1.357
D(7H–6O)	1.678	2.523	3.201	0.972
D(32O–1Mg)	1.965	2.041	2.114	
D(11O–33H)	0.997	1.516	2.404	
D(26C–33H)	3.655	1.262	1.096	
α (32O–30C–31O)	124.3	146.3	177.7	122.47
α (30C–31O–33H)	133.3	53.3	75.2	105.89

D is the bond distance in angstroms (Å) and α is the bond angle

The labeling of atoms in the first four rows represents AA atoms in the gas phase (Fig. 3), and the atoms in the remaining rows represent AA absorbed on magnesium hydroxide (Fig. 5)

cluster system shows similar binding sites as in $n = 5$ in [Mg(OH)$_2$]$_n$ nanoclusters, the dihedral angle of O–C–O–H in AA is significantly different in both systems (Fig s2 and Table s3). Remarkably, a similar configuration is also observed for the adsorption of

propionic acid (PA) on a [Mg(OH)$_2$]$_5$ nanocluster, which is shown in Structure 4 in Fig. 2.

The calculated absorption energy for PA is − 245 kJ/mol with the B3LYP/DGDZVP exchange functional and basis set, which is close to the adsorption energy of AA (− 242 kJ/mol) using the same basis set and exchange functional. The hydroxyl hydrogen of PA binds to the oxygen of [Mg(OH)$_2$]$_5$ just as it does for AA with a similar C–O–H bond angle of 133° and the presence of an intervening pair of Mg and O atoms between the bonding sites. This highlights their possible significance for providing a potentially similar mechanistic pathway for decarboxylation of the acid to form CO$_2$ and ethane (CH$_3$CH$_3$) in the presence of the [Mg(OH)$_2$]$_5$ catalyst.

Next, we move from structural details to the mechanistic pathways for the decarboxylation of AA in the gas phase, followed by a discussion of the desired reaction in the presence of (MgO)$_4$ and [Mg(OH)$_2$]$_5$ nanoclusters that function as catalysts.

Decomposition of AA in the gas phase: geometrical and polarization changes

To make a detailed comparison of the same reaction in the presence of [Mg(OH)$_2$]$_5$ and (MgO)$_4$ catalysts at the same theoretical level, the gas-phase
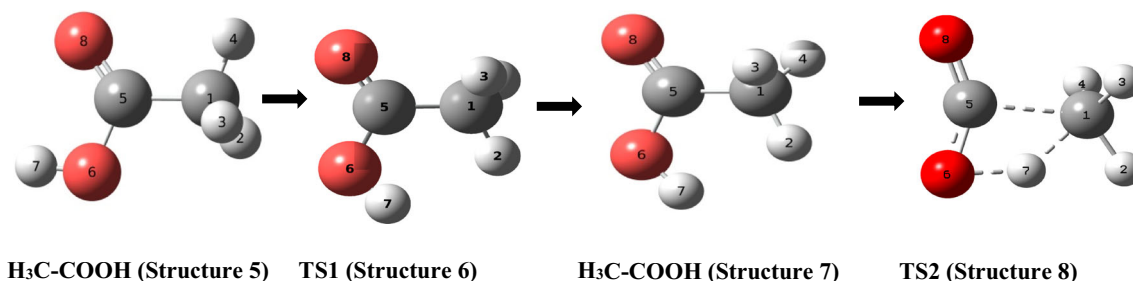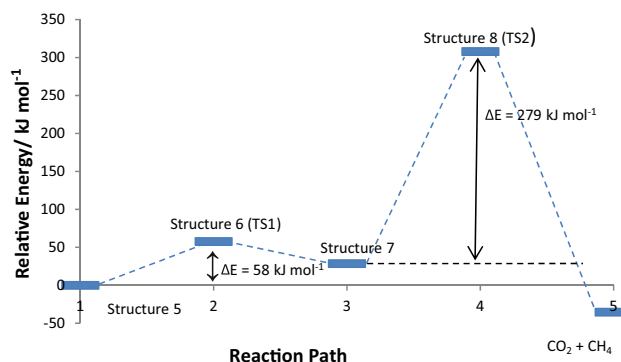
Figure 3 AA (Structure 5), transition state (TS1) for isomerization (Structure 6) isomer of AA (Structure 7), and the transition-state (TS2) structure for the gas-phase decomposition of AA (Structure 8).

decarboxylation of AA in the absence of a catalyst using DFT with the B3LYP/6-31G(*d,p*) exchange functional and basis set was studied; this highlighted the differences in their mechanistic pathways. The decarboxylation pathway was followed by tracking the intrinsic reaction coordinates after determining the transition and intermediate states [36, 37]. Figure 3 shows the reaction path for the decarboxylation of AA in the gas phase, which occurs by passing over two transition states (TS1 and TS2) and an intermediate (Structure 7). The rotational rearrangement of the equilibrated native-state Structure 5 of AA to an isomerized intermediate Structure 7 after passing over the first TS barrier (TS1), shown as Structure 6 in Fig. 3 (imaginary frequency of -813.4 cm^{-1}), brings the H atom on the OH group closer to the C atom of the CH$_3$ group. From here, it is favorably poised to form CH$_4$, after passing over the second TS (TS2). This pathway was calculated using the STQN method [38].

Our calculations show that the cis–trans isomerization of the OH group for the reorientation of AA from Structure 5 to the intermediate Structure 7 occurs through TS1 (Structure 6), with an energy barrier of ~ 57 kJ/mol. This is smaller than the barrier of 279 kJ/mol (Table 3) to reach TS2, from Structure 8 from Structure 7, before formation of the final CO$_2$ and CH$_4$ products.

Figure 4 Gas-phase AA decarboxylation via intermediate H$_3$C–COOH Structure 7.

The decarboxylation of AA in the gas phase from the initial state (Structure 5) passes over the first transition state (TS1) to the intermediate Structure 7. Final products occur via the second transition state TS2 (Structure 8 in Fig. 3), as shown schematically in Fig. 4. The energy barrier for the last step of the reaction was 279 kJ/mol at 298 K. The total barrier with respect to the initial Structure 5 was 308 kJ/mol at 298 K. The experimentally observed values from a kinetic study in a single-pulse shock tube where AA was diluted with Argon were 271.5–295.0 kJ mol^{-1} at temperatures between 1300 and 1950 K [43]. An earlier theoretical calculation predicted an activation

Table 3 Total and relative energies at 298 K with respect to Structure 5 for gas-phase AA decarboxylation

Structure	Total energy/kJ mol^{-1} DFT-B3LYP(6-31G(*d,p*))	Relative energy/kJ mol^{-1}
H$_3$C–COOH (5)	-601479.7	0
TS1 (6)	-601422.0	57.7
H$_3$C–COOH (7)	-601451.1	28.6
TS2 (8)	-601171.7	308.0
CH$_4$ + CO$_2$	-601515.1	-35.4

energy of 301 kJ mol⁻¹ at 298 K using the QCISD(TC)/6-311 ++G(d,p) level of theory [6].

Passage through an intermediate was also observed in our DFT calculations for AA decarboxylation in the presence of the [MgO]₄ catalyst [18].

The labeled Structures 5–8 are shown in Fig. 3.

In the following section, we find from our theoretical DFT calculations that the [Mg(OH)₂]₅ catalyst enables the decarboxylation AA to proceed directly without passing through an intermediate similar to what is observed in the gas phase and in the presence of the [MgO]₄ catalyst. The reasons for this are revealed from our theoretical studies of the reaction pathways.

Mechanistic pathway for the decarboxylation of AA and PA on the [(Mg(OH)₂]₅ catalytic cluster

The pathway for the decarboxylation reaction of AA adsorbed on the [Mg(OH)₂]₅ nanocluster is of interest following our description of the same reaction in the gas phase and in the presence of the [MgO]₄ catalyst [18]. Instead of the need to reorganize the adsorbed AA into an intermediate isomer, as in the gas phase or in the presence of [MgO]₄ catalyst, the AA adsorbed on the [Mg(OH)₂]₅ nanocluster (Structure 3 in Figs. 2 and 5) already has an H atom (33H) of the carbonyl hydroxyl group of the acid aligned favorably with the oxygen atom (11O) of a hydroxide group of the catalyst. This favorable alignment allows for transformation into the TS Structure 9 (Fig. 5) for conversion to CH₄ and CO₂ (Structure 9). During the final stage of decarboxylation, the proton (33H) from the carboxylic group is transferred to the methyl group with the breaking of the 30C–26C bond of the acid to form CH₄ and CO₂. The magnesium hydroxide nanocluster, thus, provides a simple and facile
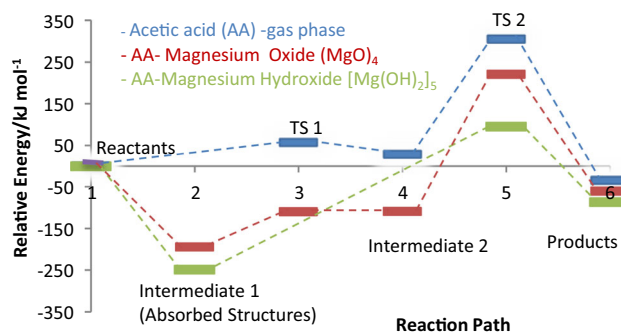
Figure 6 Schematic representation of relative energy for the adsorption and decarboxylation of AA on the [Mg(OH)₂]₅ cluster (green), on (MgO)₄ cluster (red), and AA itself (blue) with respect to IRC for the 6-31G(d,p) basis set with B3LYP exchange functional.

pathway for decarboxylation that is unique for $n = 5$, and the catalyst acts as a destructive adsorbent.

The energetics of the pathway from the reactants to products calculated with and without the dispersion corrected B3LYP–GD3 functional as shown in Fig. 6 are displayed in Table 4 with the relevant energies for Structures 3 and 9 and the final product state. According to the energy data in Table 4, the decarboxylation process of AA approach through a strong adsorption (− 251 kJ mol⁻¹) on [(Mg(OH)₂]₅ cluster and with 348 kJ mol⁻¹ decomposition energy. The relative energies in Table 4 illustrate that the adsorption is a destructive with 97 kJ mol⁻¹ as the required net energy to overcome the TS to generate the final products. This net energy is comparatively smaller than in the presence of (MgO)₄ clusters (132 kJ/mol) [18] and in the gas phase (290 kJ/mol).

The AIM method [18] was used to further characterize the bond interactions during the reaction. In an AIM calculation, a molecule is considered both classically as a collection of atoms and bonds and quantum mechanically as nuclei and electrons.

(a) Structure 3 (absorbed state)   **(b)** Structure 9 (TS)   **(c)** Structure 10 (products)
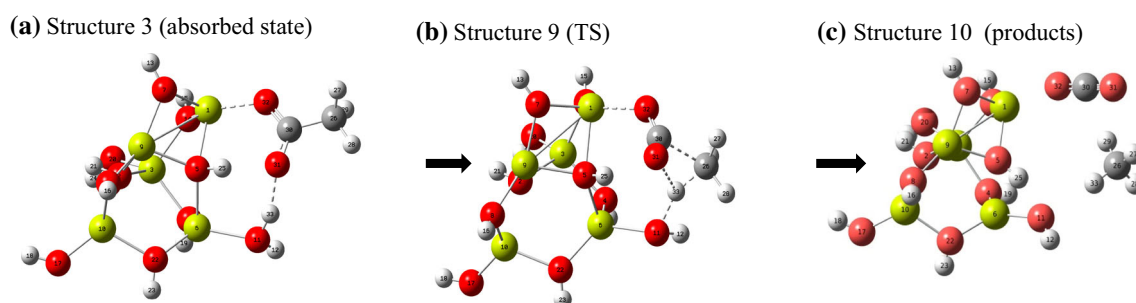
Figure 5 **a** Adsorbed AA on [(Mg(OH)₂]₅ cluster (Structure 3), **b** TS (Structure 9) for AA decomposition on [(Mg(OH)₂]₅, **c** products of the decarboxylation of AA CH₄ and CO₂ on [(Mg(OH)₂]₅ (Structure 10).

Table 4 Total and relative energies at 298 K for gas-phase AA and $[(Mg(OH)_2)]_5$ reaction using DFT with the B3LYP/6-31G(d,p) functional and basis set

Structure	Total energy/kJ mol^{-1} DFT-B3LYP(6-31G(d,p))	Relative energy/kJ mol^{-1}
AA + $[(Mg(OH)_2)]_5$	− 5221061.1 (− 5221218.5)	0 (0)
Structure 3 (adsorbed state)	− 5221311.7 (− 5221449.7)	− 250.6 (− 231.2)
Structure 9 (TS)	− 5220964.3 (− 5221121.5)	96.8 (97.0)
Structure 10 (products)	− 5221148.0 (− 5221292.6)	− 86.9 (− 74.1)

Dispersion corrected values are in parenthesis

Table 5 Electron density ρ(a.u) and Laplacian of electron density $\nabla^2\rho$ (a.u) for Structure 3, Fig. 2 adsorbed on $[Mg(OH)_2]_5$ and gas-phase AA (in parenthesis) at the B3LYP/6-31G(d,p) level of DFT from AIM calculations

Bond/characteristic	ρ	$\nabla^2\rho$
26C–30C	0.259 (0.262)	− 0.647 (− 0.659)
31O–25H	0.037	0.102
31O–30C	0.369 (0.298)	− 0.221 (− 0.471)
32O–30C	0.354 (0.416)	− 0.291 (0.172)
31O–33H	0.044 (0.358)	0.137 (− 2.056)
33H–11O	0.319	− 1.864
32O–1Mg	0.047	0.375
25H–5O	0.333	− 1.864

Atoms 1Mg, 25H, 5O, and 11O are part of the $[Mg(OH)2]5$ cluster. The rest belong to AA. Atoms 30C, 31O and 32O, and 33H form the carbonyl group of AA which decomposes to CO2 and CH4 formed with 26C and 33H, 27H, 28H, and 29H after weakening the 31O–33H bond in AA. See Table 6 and Fig. 2, Structure 3

Table 6 Electron density ρ(a.u), Laplacian of electron density $\nabla^2\rho$ (a.u) values for the TS (Structure 9) at the B3LYP/6-31G(d,p) level of DFT from AIM calculations

Bond/characteristic	ρ (au)	$\nabla^2\rho$
26C–30C	0.072	0.046
31O–30C	0.435	0.492
32O–1Mg	0.035	0.271
33H–11O	0.082	0.119
33H–26C	0.179	− 0.434
33H–31O	No BCP defined	–

BCP bond critical point

Molecular bonds in each structure are characterized by the first derivative of the electron density at the critical point equal to zero, and by the second derivative, which is the Laplacian of the density [18, 44–49]. This theory has been used to characterize bond types and studies have concluded that it is reliable, in the absence of bifurcation [50–52].

The electron and Laplacian electron densities in Table 5 reveal a strong covalent bond between an acidic hydrogen (33H) of AA and an oxygen atom (11O) in the $[(Mg(OH)_2)]_5$ cluster, and a weaker interaction between the carbonyl oxygen (32O) atom of AA and a magnesium atom (1 Mg) of the magnesium hydroxide catalyst (Structure 3 in Fig. 5). Both are shown circled in Fig. 2c to highlight the locations of the binding between the acid and catalyst, which in this case is separated by two intervening atoms, 6O and 5 Mg, on the catalyst, unlike the adjacent binding sites for the corresponding $(MgO)_4$ nanocatalyst with

the same acid. The electron density of the O–H bond in the carbonyl group of the acid interacting with the $[Mg(OH)_2]_5$ reduced from 0.358 a.u to 0.044 a.u, and the sign of the Laplacian density changed from negative to positive (− 2.0 a.u–0.14 a.u) signifying a weakening of the bond. A low (0.04 a.u) electron density, positive Laplacian density (0.3 a.u), and a longer bond Mg–O distance (1.98°A) indicate a weak ion–dipole interaction. Following adsorption, both the acidic C–O bonds to $[Mg(OH)_2]_5$ cluster tend to have similar geometries and electron densities (C–O distances of 1.2°A, electron densities of 0.3 a.u and Laplacian densities of − 0.2 a.u).

In the forward scan, the TS broke down into CO_2 and CH_4, but in the reverse scan reverts to Structure 3 in Figs. 2c and 5a, which is the optimized structure of AA adsorbed on $[Mg(OH)_2]_5$. Electron densities and the Laplacian of the electron densities of the TS (Structure 9) determined from the AIM calculations (Table 6) show a pathway for product formation from the TS, as discussed below.

This shows a weakening of the carbon–carbon single bond of AA in the TS (Fig. 5b). In addition, the electron density between 33H and 26C is 0.179 a.u., the Laplacian of the density is negative (− 0.43 a.u.) in the TS and the distance between 33H and 26C is reduced from 3.65 in Structure 3 to 1.26°A in Structure 9, revealing

Table 7 ChelpG atomic charges of the structure 3 [(Mg(OH)$_2$)$_5$-AA] and AA calculated via DFT with the B3LYP/6-31G(d,p) level of theory

Atom/characteristic	(M(OH)$_2$)$_5$AA	AA
26C	− 0.273	− 0.292
30C	0.759	0.697
31O	− 0.644	− 0.574
32O	− 0.711	− 0.529
33H	0.401	0.404
27H	0.104	0.104
28H	0.067	0.104
29H	0.077	0.084

The electron density between 26C and 30C reduced from 0.24 to 0.07 a.u., the Laplacian density changed from − 0.5 to 0.04 a.u., and the bond distance elongated from 1.53 to 2.07°A

the first steps in the formation of C–H bond in methane. Furthermore, there is a progressive change in the bond angle of 32O–30C–31O from 124.3° to 146.2° to 177.7° during the transformation from Structure 3 to 9 and then to the product 10, respectively. This indicates the formation of an O–C–O bond in CO$_2$ as a product of the decarboxylation of AA from the adsorbed state (Structure 3 in Figs. 2b and 5a). Along the pathway to the products, a new bond is observed between 33H and 26C, and the bond between 26C and 30C breaks to form methane. The CHelpG method is an atomic charge calculation system developed by Breneman and Wiberg [39]. In this method, the atomic charges are fitted to reproduce the molecular electronic potential at a number of points around the molecule. CHelpG charges, unlike Mullikan charges, depend much less on the underlying theoretical method used to compute the wave function. The atomic charge on the hydroxyl hydrogen of AA does not change significantly, but the atomic charges on the hydroxyl and carbonyl oxygen changed by 0.2 and 0.1, respectively (Table 7).

Comparison of the decarboxylation of AA in the gas phase and in the presence of (MgO)$_4$ and [Mg(OH)$_2$]$_5$ catalysts

Figure 6 shows the comparison of the energies of the intermediate and TSs along their respective reaction pathways for the decarboxylation of AA in the gas phase and separately for the corresponding reaction in the presence of the (MgO)$_4$ and [Mg(OH)$_2$]$_5$ catalysts. The figure highlights the differences in the
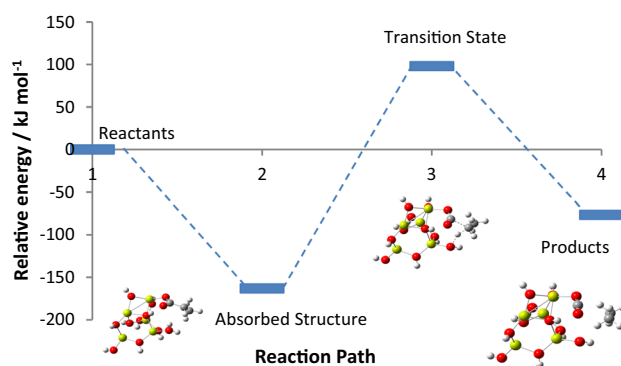
Figure 7 Schematic representation of the relative energies of adsorption and decarboxylation of PA on the [Mg(OH)$_2$]$_5$ cluster using B3LYP/6-31G(d,p).

pathways to form CO$_2$ and CH$_4$ from AA and shows that decarboxylation of AA in the gas phase and from the adsorbed state on (MgO)$_4$ passes through two transition states (TS1 and TS2), with an intermediate in between the two before ending as products.

AA adsorbed on [Mg(OH)$_2$]$_5$ clearly bypasses the intermediates and passes through the single transition state (TS1) before formation of the products. This is attributed to the absorbed state being favorably oriented, via directed chemical bonding on the cluster, to pass directly to the transition state for decarboxylation without passing through an intermediate. Calculations for $n = 1$ and 3, the following two most stable [Mg(OH)$_2$]$_n$ adsorbents for AA after $n = 5$, show that decarboxylation occurs through an intermediate and two TSs for these systems, unlike the $n = 5$ cluster. The passage from the reactant to products during the decarboxylation of AA is unique for the $n = 5$ catalyst among the investigated set of [Mg(OH)$_2$]$_n$ clusters ($n = 1$–9).

Because the absorption of PA and AA on [Mg(OH)$_2$]$_5$ is similar, as shown in Fig. 2c, d, the decarboxylation of PA to CO$_2$ and CH$_3$CH$_3$ from the adsorbed state can also be expected to pass through a single TS without an intervening intermediate. This was confirmed by tracking the pathway from the reactants to products for PA using the same methods as for AA, and the results for PA are shown in Fig. 7.

Conclusion

In this work, DFT calculations were used to select a catalyst for the decarboxylation of acetic acid (AA) from several magnesium hydroxide nanocluster [Mg(OH)$_2$]$_n$ candidates that have potential use as

coatings for textiles. It was observed that AA more strongly adsorbed on the magnesium hydroxide cluster with $n = 5$ ($E_{ad} = -252$ kJ/mol) than on the other magnesium hydroxide clusters ($n \neq 5$) or on $(MgO)_4$ ($E_{ad} = -198$ kJ/mol). The energetics and pathways for the decarboxylation of AA in the gas phase were compared with the same reaction in the presence of strongly adsorbing $[Mg(OH)_2]_5$ and $(MgO)_4$ clusters [18], and particular attention was given to the adsorption stereochemistry. The theoretical analysis revealed that the decarboxylation reaction pathway for AA passes through an intermediate between two TSs in both absence of a catalyst [5, 6] and when it occurs in the presence of the $(MgO)_4$ catalyst [18]. However, for the $[Mg(OH)_2]_5$ catalyst, the structure and orientation of the AA absorbed on $[Mg(OH)_2]_5$ enable it to bypass the intermediate observed for the other cases. We hypothesized and confirmed that a similar pathway existed for the decarboxylation of propionic acid (PA) with the same catalyst. The experimental implementation of decarboxylation with the $[Mg(OH)_2]_5$ catalyst, however, would require precise synthesis of $n = 5$ nanoclusters because the other nanoclusters do not share the same stereospecific catalytic properties for the decarboxylation of AA and PA.

Acknowledgements

Compliance with ethical standards

Conflict of interest The authors declare no conflict of interest.

Electronic supplementary material: The online version of this article (https://doi.org/10.1007/s108 53-020-05196-z) contains supplementary material, which is available to authorized users.

References

[1] Alonso DM, Bond JQ, Dumesic JA (2010) Catalytic conversion of biomass to biofuels. Green Chem 12:1493–1513

[2] Saidi M, Samimi F, Karimipourfard D, Nimmanwudipong T, Gates BC, Rahimpour MR (2014) Upgrading of lignin-derived bio-oils by catalytic hydrodeoxygenation. Energy Environ Sci 7:103–129

[3] Shibata T, Nishiyama H (2014) Acetic acid decomposition in a coaxial dielectric barrier discharge tube with mist flow. Plasma Chem Plasma Process 34:1331–1343

[4] Blake PG, Jackson GE (1968) The thermal decomposition of acetic acid. J Chem Soc B. https://doi.org/10.1039/J29680001153

[5] Blake PG, Jackson GE (1969) High- and low-temperature mechanisms in the thermal decomposition of acetic acid. J Chem Soc B. https://doi.org/10.1039/J29690000094

[6] Bamford CH, Dewar MJS (1949) The thermal decomposition of acetic acid. J Chem Soc. https://doi.org/10.1039/JR9490002877

[7] Ruelle P (1986) Ab initio quantum-chemical study of the unimolecular pyrolysis mechanisms of acetic acid. Chem Phys 110:263–274

[8] Nguyen MT, Ruelle P (1987) Comment on ab initio quantum-chemical study of the unimolecular pyrolysis mechanisms of acetic acid. Chem Phys Lett 138:486–488

[9] Nguyen MT, Sengupta D, Raspoet G, Vanquickenborne LG (1995) Theoretical study of the thermal decomposition of acetic acid: decarboxylation versus dehydration. J Phys Chem 99:11883–11888

[10] Li XB, Wang SR, Zhu YY, Yang GH, Zheng PJ (2015) DFT study of bio-oil decomposition mechanism on a Co stepped surface: acetic acid as a model compound. Int J Hydrogen Energy 40:330–339

[11] Neitzel A, Lykhach Y, Johanek V, Tsud N, Skala T, Prince KC, Matolin V, Libuda J (2014) Role of oxygen in acetic acid decomposition on Pt(111). J Phys Chem C 118:14316–14325

[12] Grinter DC, Nicotra M, Thornton G (2012) Acetic acid adsorption on anatase TiO_2(101). J Phys Chem C 116:11643–11651

[13] Hamid S, Dillert R, Bahnemann DW (2018) Photocatalytic reforming of aqueous acetic acid into molecular hydrogen and hydrocarbons over co-catalyst-loaded TiO_2: shifting the product distribution. J Phys Chem C 122:12792–12809

[14] Liao LF, Lien CF, Lin JL (2001) FTIR study of adsorption and photoreactions of acetic acid on TiO_2. Phys Chem Chem Phys 3:3831–3837

[15] Martin C, Martin I, Rives V (1992) An FT-IR study of the adsorption of pyridine, formic acid and acetic acid on magnesia and molybdena-magnesia. J Mol Catal 73:51–63

[16] Verma AM, Kishore N (2018) Decomposition of acetic acid over Ru and Ru/MgO catalyst clusters under DFT framework. Chem Phys Lett 711:156–165

[17] Verma AM, Kishore N (2018) Kinetics of decomposition reactions of acetic acid using DFT approach. Open Chem Eng J 12:14–23

[18] Perera DC, Hewage JW, De Silva N (2015) Theoretical study of catalytic decomposition of acetic acid on MgO nanosurface. Comput Theor Chem 1064:1–6

[19] Xiaohong P, Wang Y, Chen Z, Pan D, Cheng Y, Liu Z, Lin Z, Guan X (2013) Investigation of antibacterial activity and related mechanism of a series of nano-$Mg(OH)_2$. ACS Appl Mater Interfaces 5(3):1137–1142

[20] Halbus AF, Horozov TS, Paunov VN (2019) Controlling the antimicrobial action of surface modified magnesium hydroxide nanoparticles. Biomimetics 4(2):41

[21] Wang YR, Liu FJ (2013) Progress on the preparation and application of Mg $(OH)_2$ as new flame retardants. Appl Mech Mater 320:259–264

[22] Weizhen L, Huang F, Wang YJ, Zou T, Zheng J, Lin Z (2011) Recycling $Mg(OH)_2$ nanoadsorbent during treating the low concentration of CrVI. Environ Sci Technol 45(5):1955–1961

[23] Ding Y, Zhang G, Wu H, Hai B, Wang L, Qian Y (2001) Nanoscale magnesium hydroxide and magnesium oxide powders: control over size, shape and structure via hydrothermal synthesis. Chem Mater 13:435–440

[24] Chen Y, Zhou T, Fang H, Li S, Yao Y, He Y (2015) A novel preparation of nano-sized hexagonal $Mg(OH)_2$. Proc Eng 102:388–394

[25] Wu J, Yan H, Zhang X, Wei L, Liu X, Xu B (2008) Magnesium hydroxide nanoparticles synthesized in water-in-oil microemulsions. J Colloid Interface Sci 324:167–171

[26] Sun Q, Chen B, Wu X, Wang M, Zhang C, Zeng X, Wang J, Chen J (2015) Preparation of transparent suspension of lamellar magnesium hydroxide nanocrystals using a high-gravity reactive precipitation combined with surface modification. Ind Eng Chem Res 54:666–671

[27] Wang SY, Li GM, Xu W, Liu C, Dai L, Zhu HC (2016) Facile preparation and application of magnesium hydroxide assembly spheres. Res Chem Intermed 42:2661–2668

[28] Chen H, Xu C, Liu Y, Zhao G (2012) Formation of flower-like magnesium hydroxide microstructure via a solvothermal process. Electron Mater Lett 8:529–533

[29] An D, Ding X, Wang Z, Liu Y (2010) Synthesis of ordered arrays of magnesium hydroxide nanoparticles via a simple method. Colloids Surf A 356:28–31

[30] Al-Hazmi F, Umar A, Dar GN, Al-Ghamdi AA, Al-Sayari SA, Al-Hajry A, Kim SH, Tuwirqi RM, Alnowaiserb F, El-Tantawy F (2012) Microwave assisted rapid growth of $Mg(OH)_2$ nanosheet networks for ethanol chemical sensor application. J Alloys Compd 519:4–8

[31] Chen M, Dixon DA (2017) Structure and stability of hydrolysis reaction products of MgO nanoparticles leading to the formation of brucite. J Phys Chem C 121:21750–21762

[32] Zheng J, Zhou W (2013) Low temperature synthesis of nanoscale magnesium hydroxide under normal pressure. Adv Mater Res 779–780:247–250

[33] Koper O, Klabunde KJ, Martin LS, Knappenberger KB, Hladky LL, Decker SP (2003) Reactive nanoparticles as destructive adsorbents for biological and chemical contamination. United States US6653519B2

[34] Vaiss VS, Borges I Jr, Leitao AA (2011) Sarin degradation using brucite. J Phys Chem C 115:24937–24944

[35] Grimme S, Antony J, Ehrlich S, Krieg H (2010) A consistent and accurate ab initio parametrization of density functional dispersion correction (DFT-D) for the 94 elements H-Pu. J Chem Phys 132:154104

[36] Fukui K (1981) The path of chemical reactions—the IRC approach. Acc Chem Res 14:363–368

[37] Maeda S, Harabuchi Y, Ono Y, Taketsugu T, Morokuma K (2015) Intrinsic reaction coordinate: calculation, bifurcation and automated search. Int J Quantum Chem 115:258–269

[38] Peng C, Schlegel HB (1993) Combining synchronous transit and quasi-Newton methods for finding transition states. Israel J Chem 33:449–454

[39] Breneman CM, Wiberg KB (1990) Determining atom-centered monopoles from molecular electrostatic potentials. The need for high sampling density in formamide conformational analysis. J Comput Chem 11:361–373

[40] Zhao Z, Rogers DM, Beck TL (2010) Polarization and charge transfer in the hydration of chloride ions. J Chem Phys 132:014502

[41] Bader RWF (1990) Atoms in molecules: a quantum theory. Oxford University Press, Oxford

[42] Frisch MJ, Trucks GW, Schlegel HH, Scuseria GE, Robb MA, Cheeseman JR, Scalmani G, Barone V, Mennucci B, Petersson GA, Nakatsuji H, Caricato M, Li X, Hratchian HP, Izmaylov AF, Bloino J, Zheng G, Sonnenberg JL, Hada M, Ehara M, Toyota K, Fukuda R, Hasegawa J, Ishida M, Nakajima T, Honda Y, Kitao O, Nakai H, Vreven T, Montgomery JA Jr, Peralta JE, Ogliaro F, Bearpark M, Heyd J, Brothers E, Kudin KN, Staroverov VN, Kobayashi R, Normand J, Raghavachari K, Rendell A, Burant JC, Iyengar SS, Tomasi J, Cossi M, Rega N, Milliam JM, Klene M, Knox JE, Cross JB, Bakken V, Adamo C, Jaramillo J, Gomperts R,

Stratmann RE, Yazyev O, Austin AJ, Cammi R, Salvador CP, Dannenberg JJ, Dapprich S, Daniels AD, Farkas O, Foresman JB, Ortiz JV, Cioslowski J, Fox DJ (2009) Gaussian 09, Revision D.01. Gaussian Inc, Wallingford CT

[43] Mackie JC, Doolan KR (1984) High-temperature kinetics of thermal decomposition of acetic acid and its products. Int J Chem Kinet 16:525–541

[44] Michalkova A, Ilchenko M, Gorb L, Lesczynski J (2004) Theoretical study of the adsorption and decomposition of sarin on magnesium oxide. J Phys Chem B 108:5294–5303

[45] Oliva JM, Allan NL, Schleyer PVR, Vinas C, Teixidor F (2005) Strikingly long C–C distances in 1,2-disubstituted ortho-carboranes and their dianions. J Am Chem Soc 127:13538–13547

[46] Grabowski SJ (2001) An estimation of strength of intramolecular hydrogen bonds-ab initio and AIM studies. J Mol Struct 562:137–143

[47] Mahadevi AS, Neela YI, Sastry GN (2012) Hydrogen bonded networks in formamide $[HCONH_2]_n$ ($n = 1$–10) clusters: a computational exploration of preferred aggregation patterns. J Chem Sci 124:35–42

[48] Cheeseman JR, Carroll MT, Bader RFW (1988) The mechanics of hydrogen bond formation in conjugated systems. Chem Phys Lett 143:450–458

[49] Carroll MT, Chang C, Bader RFW (1988) Predictions of the structures of hydrogen-bonded complexes using the Laplacian of the charge density. Mol Phys 63:387–405

[50] Srivastava AK, Misra N (2014) Calculating interaction energies of hydrogen bonded dimers and complexes of HF, H_2O and NH_3: super-molecular versus AIM approach. J Comput Methods Mol Des 4:19–23

[51] Hobza P, Sponer J, Cubero E, Orozco M, Luque FJ (2000) C–H–O contacts in the adenine—uracil Watson—Crick and uracil—uracil nucleic acid base pairs: nonempirical ab initio study with inclusion of electron correlation effects. J Phys Chem B 104:6286–6292

[52] Shishkin OV, Gorb L, Leszczynski J (2000) Modelling of the hydration shell of uracil and thymine. Int J Mol Sci 1:17–27